How to cite: *Angew. Chem. Int. Ed.* **2026**, *65*, e19825
doi.org/10.1002/anie.202519825

Electrosynthesis **Very Important Paper**

Electrolyte-Free Electrosynthesis of Pure H_2O_2 via Triple-Phase Interface Engineering

Xinxin Li, Cheng Tang, Linchuan Cong, Kaijie Wu, Jinhui Liu, Changli Wang, Eugenia Angelica, Sheng Chen, and Qiang Zhang**

Abstract: Electrosynthesis of pure H_2O_2 through proton exchange membrane electrolyzers offers a promising route for decentralized, on-demand production. However, conventional approaches face critical challenges in balancing O_2 supply and H_2O_2 removal at the gas–liquid–solid interface. In this study, we propose a triple-phase interface engineering strategy by integrating a three-dimensional (3D) hydrophobic grid gas diffusion electrode (GDE) with gas–liquid two-phase flow. This design achieves a peak Faradic efficiency (FE) of 84.6% at −10.0 mA cm^{-2} using deionized water as the catholyte. Simulations reveal that bubble wake-induced toroidal vortices enhance O_2 transport, while shear-driven convection accelerates directional H_2O_2 transport. Integrated with a T-junction microfluidic unit, it achieves real-time organic pollutant degradation while maintaining an FE above 60% over 50 h. The system demonstrates high flexibility, scalability (25 cm^2 electrode), and tunable H_2O_2 concentrations (153.6–2443.7 mg L^{-1}), rendering a robust platform for sustainable, on-demand chemical electrosynthesis.

Introduction

The decentralized electrochemical production of hydrogen peroxide (H_2O_2) via two-electron ($2e^-$) oxygen reduction reaction (ORR) using renewable electricity has emerged as a sustainable route for applications such as agricultural oxygenation,[1,2] water treatment,[3–5] and fine-chemical synthesis.[6,7] However, conventional H_2O_2 electrolyzers typically rely on supporting electrolytes (e.g., acids, bases, or salts) to ensure efficient ion conduction and high-yield production.[8–10] Consequently, the resultant H_2O_2 product contains significant ionic impurities, necessitating energy- and cost-intensive purification steps that undermine truly decentralized deployment.[11–13] Therefore, developing electrolysis systems capable of producing high-purity, low-ionic-content H_2O_2 solution directly from pure water remains a crucial breakthrough for sustainable application. However, pure-water electrolysis confronts three interwined challenges: i) extremely low ionic conductivity, ii) limited O_2 solubility, and iii) mass-transfer constraints at the gas–liquid–solid triple-phase interface, even when using highly selective $2e^-$ ORR catalysts.[14–16]

Replacing liquid electrolytes with solid electrolytes offers a pathway to enhance ion conduction and reduce system resistance. For example, Xia et al. proposed a three-chamber porous solid electrolyte (PSE) reactor, where ions were conducted through a porous solid electrolyte layer, enabling the combination of HO_2^- and H^+ to produce pure H_2O_2 at concentrations up to 20 wt%.[17] While this system demonstrates scalability advantages, it suffers from high internal resistance, complex assembly, and insufficient durability of components.[18,19] Proton exchange membranes (PEMs) eliminate the need for added electrolytes by shuttling protons from the anodic oxygen evolution reaction (OER) to the cathode via the Grotthuss and Vehicle mechanisms.[20–22] Recently, Chen et al. successfully demonstrated stable, continuous operation for 200 h at industrial current densities (400 mA cm^{-2}), achieving up to 7 wt% pure H_2O_2.[23] However, in compact zero-gap PEM configurations, the $2e^-$ ORR is confined to the triple-phase interface, where sluggish mass transfer of O_2 (g) and H_2O_2 (l) severely limits performance (Figure 1a). Supplying O_2-saturated water (~1.8 mM) to the cathode yields a Faradic efficiency (FE) of only 1.4%, while gas-phase O_2 feedstocks (~43 mM) produce only microliter-scale H_2O_2 due to trace water diffusion across the membrane.[24] Thus, simultaneously overcoming the limitations concerning O_2 supply, ion conduction, and product extraction at the triple-phase interface is essential to unlock efficient electrolyte-free synthesis.

[*] Dr. X. Li, Prof. C. Tang, Dr. L. Cong, K. Wu, J. Liu, C. Wang, E. Angelica, Prof. Q. Zhang
Tsinghua Center for Green Chemical Engineering Electrification, Department of Chemical Engineering, Tsinghua University, Beijing 100084, P.R. China
E-mail: cheng-net0@tsinghua.edu.cn
zhang-qiang@mails.tsinghua.edu.cn

Prof. C. Tang, Prof. Q. Zhang
State Key Laboratory of Chemical Engineering and Low-Carbon Technology, Tsinghua University, Beijing 100084, P.R. China

Prof. C. Tang, Prof. Q. Zhang
Institute for Carbon Neutrality, Tsinghua University, Beijing 100084, P.R. China

K. Wu, Prof. S. Chen
Key Laboratory for Soft Chemistry and Functional Materials, School of Chemistry and Chemical Engineering, Nanjing University of Science and Technology, Nanjing 210094, P.R. China

Additional supporting information can be found online in the Supporting Information section

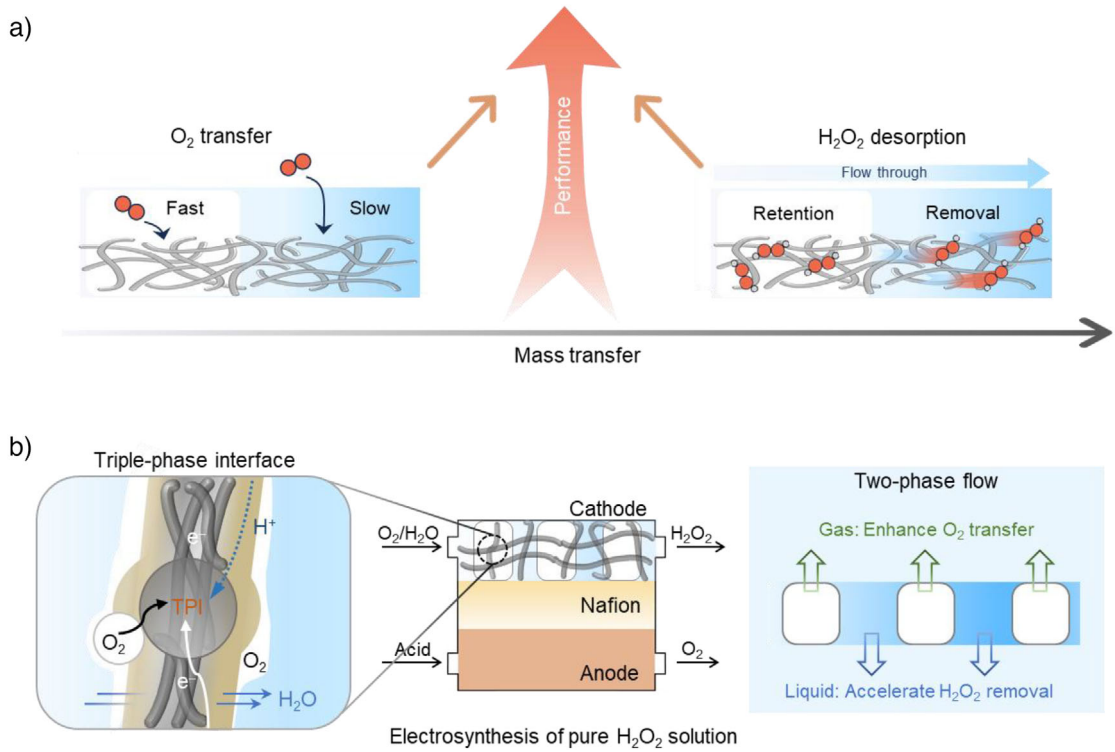

Figure 1. Triple-phase interface engineering strategy for electrosynthesis of pure H_2O_2 solution. a) The impact of O_2 and H_2O_2 mass transfer on the performance of $2e^-$ ORR. b) Integrating a 3D hydrophobic grid GDE with gas–liquid two-phase flow to overcome mass transfer bottlenecks.

In this contribution, we propose a triple-phase interface engineering strategy to overcome these mass transfer bottlenecks. By integrating a PEM structure for proton transport with a three-dimensional (3D) hydrophobic grid gas diffusion electrode (GDE), we establish favorable triple-phase interface with enhanced mass transfer channels through gas–liquid two-phase flow (Figure 1b). This design achieves a peak FE of 84.6% for H_2O_2 production in pure water at -10.0 mA cm^{-2}, with tunable H_2O_2 concentrations from 153.6 to 2443.7 mg L^{-1} on a 25 cm^2 electrode. Computational fluid dynamics (CFD) simulations validate the reliability of this approach in addressing mass transfer limitations. The system maintains FE above 60% over 50 h and when integrated with a T-junction microfluidic unit, it simultaneously achieves real-time organic pollutant degradation, demonstrating high stability, scalability, and flexibility for decentralized, high-throughput, low-concentration H_2O_2 applications.

Results and Discussion

Design of 3D Hydrophobic Grid GDE

We proposed a zero-gap PEM-GDE assembly that unites rapid proton conduction, dynamic O_2 delivery, and continuous H_2O_2 extraction (Figure 2a). In this configuration, a Nafion 117 membrane directly contacts the GDE, minimizing ionic resistance, while gas–liquid two-phase flow sustains reactant supply and product removal. To tune the triple-phase microenvironment, we compared polytetrafluoroethylene (PTFE)-modified 2D carbon paper (CP, thickness of 0.235 mm) and 3D carbon felt (CF, thickness of 2.0 mm) as different gas diffusion layers (GDLs) to construct the membrane electrode assembly (MEA). In the 2D CP-based GDE (MEA configuration), reactants flow along its surface. In contrast, in the 3D CF-based GDE (TPI-MEA configuration), reactant fluids flow through its porous framework, which creates extensive, continuous gas–liquid–solid interfaces (Figure 2a). Furthermore, an uninterrupted Taylor flow pattern, initiated at the T-junction inlet, persists throughout the electrolyzer and remains intact at the outlet (Figure 2b). This observation indirectly confirms that discrete gas bubbles are maintained within the electrode matrix.[25]

A previously established $2e^-$ ORR electrocatalyst, nitrogen, oxygen-coordinated cobalt single-atom (CoNOC) catalyst with a cobalt content of 0.2 wt%, was employed in this work.[26] High-angle annular dark field scanning transmission electron microscopy (HAADF-STEM) image confirms the atomically dispersed Co single atoms (isolated bright spots) anchored on onion-like graphitic layers (Figure S1). X-ray diffraction (XRD) pattern shows only broad graphitic peaks with no metallic Co phases (Figure S2a), and Raman spectroscopy indicates high defect density with a large intensity ratio of D and G band ($I_D/I_G = 1.15$, Figure S2b). Electrochemical tests demonstrate that CoNOC achieves a high H_2O_2 selectivity above 80% across a wide potential range from 0.2 to 0.7 V versus reversible hydrogen electrode (RHE) (Figure S3), validating its suitability for probing triple-phase interface mass transfer effects. After catalyst loading, both CoNOC/CP and CoNOC/CF electrodes exhibit

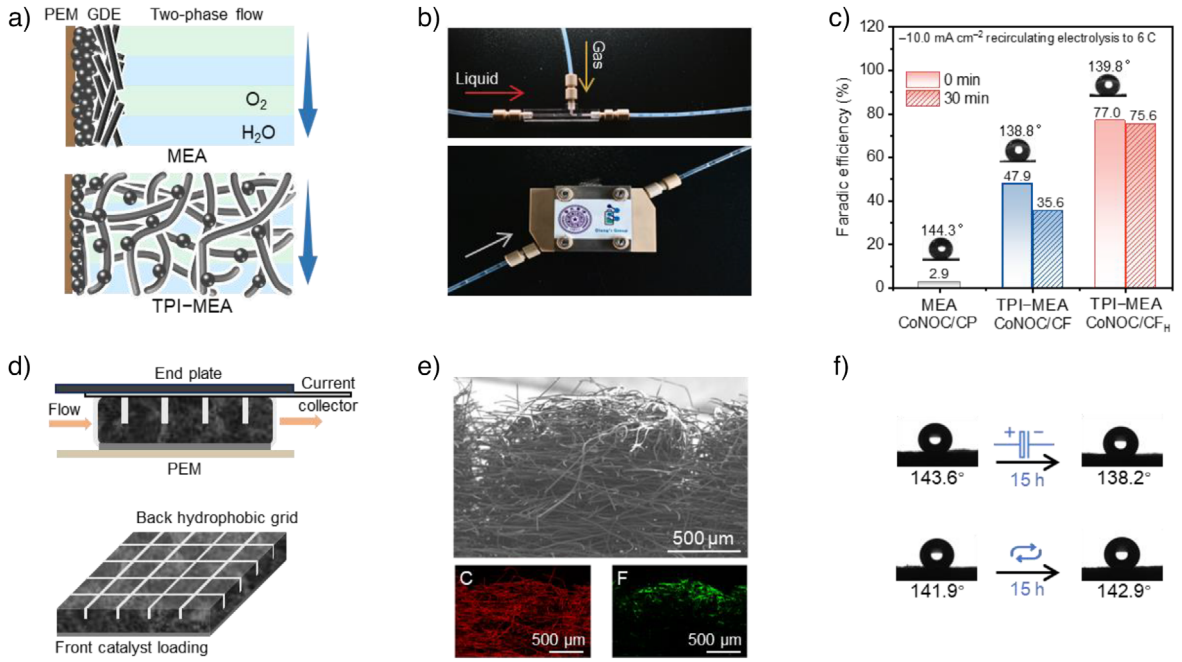

Figure 2. PEM electrolyzer with the 3D hydrophobic grid GDE. a) Electrolyzer configurations of MEA and TPI-MEA. b) Optical photos of two-phase flow O_2 supply mode. c) Performance comparison of different GDE structures. d) Schematic of the CoNOC/CF$_H$. e) Cross sectional morphology and elemental mappings of CoNOC/CF$_H$. f) Hydrophobicity tests of the CoNOC/CF$_H$ after 15 h of electrolytic and idle cycles. All tests were conducted in recirculating electrolysis.

superhydrophobicity (water contact angle > 135°, Figure 2c), attributed to the low surface energy structure formed by PTFE modification.[27] A two-phase flow, consisting of oxygen and deionized water (DI H_2O), was circulated through the cathode at flow rates of 40.0 and 16.0 mL min^{-1}, respectively. Electrochemical tests reveal that CoNOC/CP delivers a FE of only 2.9%, while CoNOC/CF achieves 47.9% (Figures 2c and S4). This performance enhancement arises from the hierarchically porous network of the 3D CF, which establishes continuous triple-phase interfaces compared to the planar structure of 2D CP.[28] However, the FE of CoNOC/CF declines to 35.6% after 30-min operation. Cross sectional F-element distribution analysis reveals a PTFE-rich surface layer that diminishes within 500 μm (Figure S5), leading to interior wetting.

To reinforce hydrophobicity, we etched a 4 × 4 grid structure (1 mm depth) into the backside of the CF (denoted as CoNOC/CF$_H$, Figure 2d). These grid-patterned grooves serve as dedicated channels to facilitate the uniform infusion of PTFE deep into the CF. Scanning electron microscopy (SEM) images show grid-patterned microcracks that facilitate PTFE infiltration (Figures 2e and S6), leading to enhanced internal PTFE coverage (Figure S7). The uniformity of the resultant hydrophobic coating was confirmed by water contact angle measurements, which show consistently high values at the catalyst side, hydrophobic side, and cross section, both before and after 5-h electrolysis (Figure S8). To confirm the superior catalyst distribution in the CF structure, a control experiment was conducted by drop-casting the catalyst ink (adding Pt/C to CoNOC ink as an external reference) onto the CF and CP. The elemental map for Pt reveals its deep and uniform penetration within the CF's 3D network (penetration depth of ~1.3 mm), in contrast to the confinement to a thin surface layer on the CP (~26 μm) (Figure S9). The optimized CoNOC/CF$_H$ achieves a high FE of 77.0% and retains the value of 75.6% after 30-min electrolysis (Figure 2c). Notably, this performance was achieved at the optimal catalyst loading of 1.5 mg cm^{-2}, which strikes the best balance between providing sufficient active sites and maintaining efficient mass transport (Figure S10a). The performance improvement is attributed to the grid-induced PTFE redistribution, which restores pore hydrophobicity, improves O_2 access, and slows GDE wetting.[29] Furthermore, the stable two-phase flow observed at the outlet confirms that the grid structure does not disrupt the primary flow path through the macroporous CF. In the TPI-MEA configuration, CoNOC/CF$_H$ remains superhydrophobic (>135°) after 15 h of electrolytic and idle cycles (Figure 2f). Notably, excess PTFE modification (>5 wt%) will induce pore blockage and shield active site, dropping FE below 50% (Figure S10b).[30]

Mass Transfer Enhancement by Two-Phase Flow

To systematically evaluate the impact of gas–liquid two-phase flow on mass transfer, we compared three distinct O_2 supply modes: i) alternating gas–liquid flow (alternating O_2/H_2O delivery, Figure 3a-i), ii) humidified O_2 (gas-phase dominant, Figure 3b-i), and iii) O_2-saturated water (liquid-phase dominant, O_{sat} H_2O, Figure 3c-i). Electrolysis at −1.29 V versus Ag/AgCl with O_2 at 40.0 mL min^{-1} and H_2O at 0.2 mL min^{-1} yields markedly different current responses. Two-phase flow

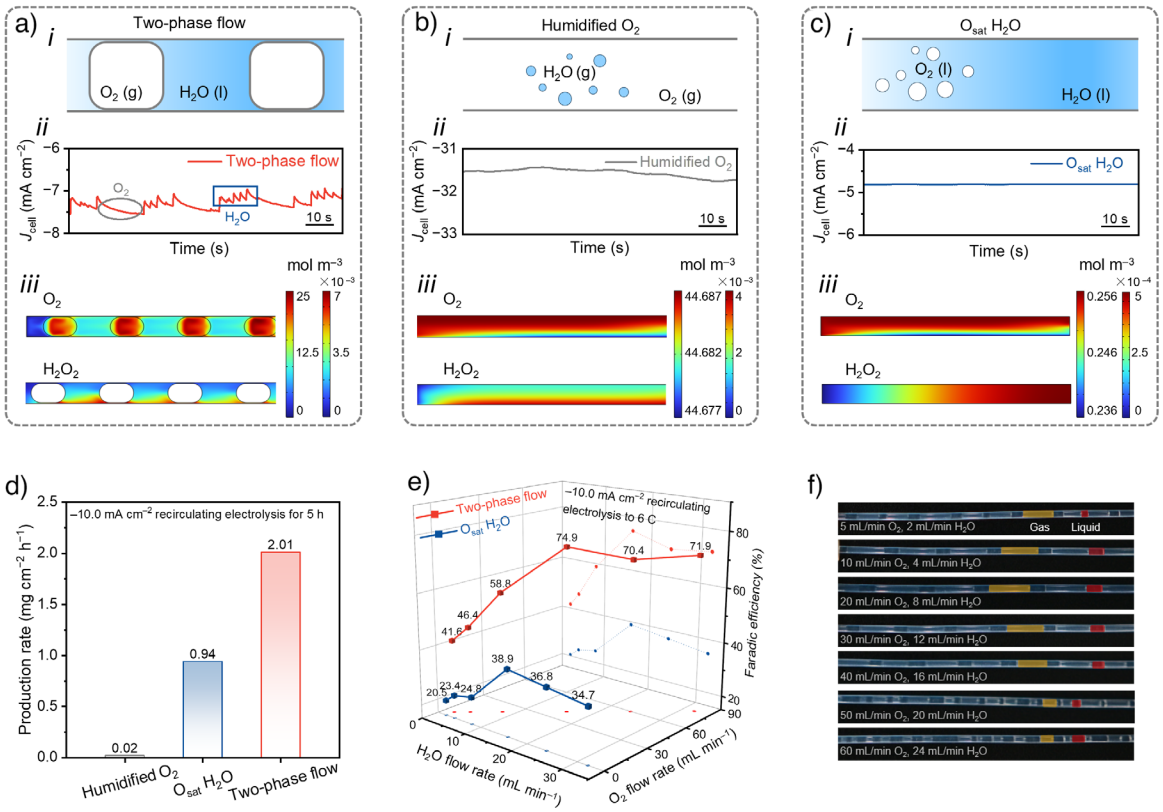

Figure 3. Mass transfer enhancement by regulating O_2 supply modes. a) Two-phase flow, b) humidified O_2, and c) O_{sat} H_2O. For each mode, i) illustrates the schematic of the O_2 supply method, ii) shows the current response under constant potential electrolysis, and iii) displays the CFD simulation of O_2 and H_2O_2 spatiotemporal distribution during electrolysis for 10 s (left colorbar: O_2 concentration distribution; right colorbar: H_2O_2 concentration distribution). d) H_2O_2 production rates of three O_2 supply modes with 40.0 mL min^{-1} O_2 and 16.0 mL min^{-1} H_2O. e) FEs of different two-phase flow configurations. f) Optical photos of different two-phase flow configurations. All tests were conducted in recirculating electrolysis mode.

produces periodic oscillations (Figure 3a-ii), whereas humidified O_2 achieves an ultrahigh current density of −31.5 mA cm^{-2} (Figure 3b-ii) and O_{sat} H_2O collapses to −4.8 mA cm^{-2} (Figure 3c-ii). Deconvolution of the periodic current signals of the two-phase flow (Figure 3a-ii) reveals that the high-current plateaus (ca. −7.5 mA cm^{-2}) coincide with bubble passages, where bubble-induced vortices enhance convective mass transfer of O_2 toward the electrode, and the low-current intervals (ca. −7.0 mA cm^{-2}) correspond to liquid slug segments, in which molecular diffusion sustains relatively high current despite partial water-film coverage of active sites.[31] This periodic current fluctuation provides indirect evidence of a stable Taylor flow pattern that continuously renews the triple-phase interface. Statistical analysis of the bubble-to-slug volume ratio at the inlet and outlet confirms the macroscopic stability of the two-phase flow, with nearly identical median values (Figure S11). Minor bubble–electrode interactions on the superhydrophobic GDE (e.g., gas adsorption/desorption) may introduce small ripples within the O_2-plateau regions, but they do not affect the dominant mechanism (Figure 3a-ii). Potentiostatic tests further confirm that these current fluctuations are governed by mass-transport dynamics rather than hydraulic resistance (Figure S12), underscoring that the two-phase flow maintains its configuration and induces periodic mass-transfer variations as it traverses the electrode.

Based on spatiotemporal distribution features of O_2 and H_2O_2, CFD simulations were further conducted to elucidate the mass transfer enhancement mechanism in the two-phase flow (Figure 3a-iii, b-iii, and c-iii). The O_2 wake-induced toroidal vortices enhance liquid-phase mixing efficiency (Figure S13),[32] thus increasing the dissolved O_2 concentration in liquid slugs by two orders of magnitude compared to single-phase liquid flow (Figure S14a,c). Concurrently, the gas–liquid interfacial shear disrupts laminar boundary layers to homogenize H_2O_2 distribution through convection compared to single-phase gas flow (Figure S15). In contrast, single-phase systems exhibit diffusion-limited transport.[33] Gas-phase mode doubles oxygen concentration relative to two-phase flow (Figure S14a,b), but develops radial H_2O_2 gradients with maximum concentration at the electrode surface (Figure 3b-iii), demonstrating constrained product removal. Liquid-phase mode shows dominant axial H_2O_2 gradients (Figure 3c-iii), indicating progressive product accumulation along the flow direction, yet suffers from severe oxygen deficiency (O_2 < 0.5 mol m^{-3}) that restricts mass transfer (Figure S14c). Thus, CFD simulations reveal that the two-phase flow overcomes key mass transfer bottlenecks by enhancing dissolved O_2 availability via wake-induced mixing and promoting H_2O_2 homogenize distribution through interfacial shear-driven convection.[34]

Consistent with these insights, the two-phase flow delivers the highest H_2O_2 production rate of 2.01 mg cm^{-2} h^{-1}, significantly outperforming humidified O_2 (0.02 mg cm^{-2} h^{-1}) and O_{sat} H_2O (0.94 mg cm^{-2} h^{-1}) (Figure 3d; Figures S16 and S17; Table S1). This outstanding production rate highlights the key advantage of the two-phase flow system, which effectively balances the trade-off between product concentration and FE. Electrochemical impedance spectroscopy (EIS) elucidates the underlying mechanism, while the two-phase flow exhibits favorable charge-transfer kinetics, overall performance is ultimately dictated by a mass-transfer process that is advantageously harnessed for continuous product extraction in this configuration (Figure S18). Although humidified O_2 achieves the highest liquid-phase H_2O_2 concentration (1051.0 mg L^{-1}), its actual production rate is severely limited by product retention. O_{sat} H_2O exhibits a lower concentration (468.3 mg L^{-1}) due to mass transfer limits, consistent with its lower ORR current observed in linear sweep voltammetry (Figure S19). The two-phase flow configuration overcomes these limitations by enabling continuous product extraction and enhanced oxygen supply, thereby achieving both a moderate concentration and a superior production rate. The two-phase flow system also maintains twice the FE of O_{sat} H_2O at −40.0 mA cm^{-2}, demonstrating exceptional mass transfer capability (Figure S20). Flow rate optimization based on repeated measurements (Figures 3e and S21) reveals that gradually increasing the flow rates of O_2/H_2O in the two-phase flow achieves a peak FE of 74.9% at 40.0/16.0 mL min^{-1}. However, exceeding critical flow rates (O_2 > 40.0 mL min^{-1} or H_2O > 16.0 mL min^{-1}) causes a slight FE decline due to unstable two-phase flow (Figure 3f).[35] Additionally, 5 h cycling tests showed FE dropping to 31.7% (Figure S17), likely attributed to H_2O_2 reduction during cycling. Further experiments confirm a 13.5% consumption of H_2O_2 via electroreduction for 1 h (Table S2), emphasizing the necessity of interface engineering strategies to minimize H_2O_2 reduction and sustain high FE.

H_2O_2 Management by 3D Flow-Through GDE

To probe how 3D flow-through architecture governs H_2O_2 removal kinetics, we compared the conventional "flow-along" MEA versus our "flow-through" TPI-MEA (Figure 4a,b). 0.10 M $HClO_4$ was used to ensure proton availability for direct performance comparison. Under single-pass electrolysis mode (O_2: 40.0 mL min^{-1}, liquid: 1.0 mL min^{-1}), the MEA configuration achieves only 79.5 mg L^{-1} H_2O_2 concentration and 3.6% FE (Figure 4c and Table S3). This inefficiency stems from inherent limitations of its 2D structure—dense CP GDL ensures O_2 transport (gas permeability: 4.5 Gurley sec for SGL 28BC) but hinders the transport of liquid-phase products across the CP. The TPI-MEA configuration, by contrast, delivers 2062.2 mg L^{-1} H_2O_2 concentration and 91.3% FE, a dramatic enhancement attributed to its superior 3D mass transfer channels. It provides expanded interfacial area, enhanced electrolyte penetration, and dynamic shear-induced desorption at the triple-phase interface.[36] When the two-phase flow passes through the electrode, the gradient-

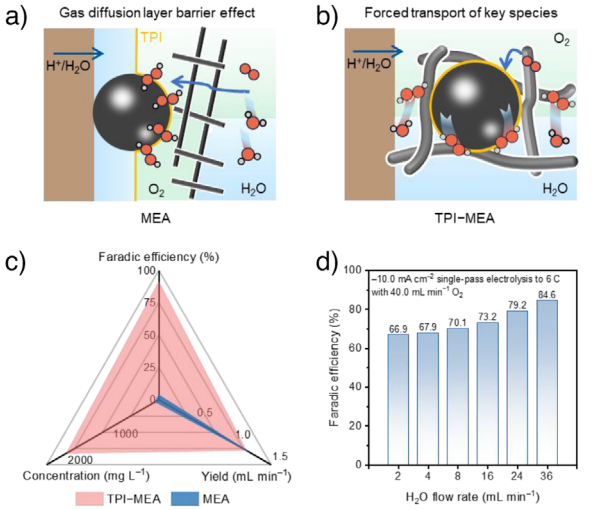

Figure 4. H_2O_2 management by different GDE architectures. Mass transport mechanism at the triple-phase interface of a) MEA and b) TPI-MEA. c) Radar chart of representative variables for different electrolyzer configurations (−50.0 mA cm^{-2} single-pass electrolysis with 40.0 mL min^{-1} O_2 and 1.0 mL min^{-1} 0.10 M $HClO_4$). d) FEs of single-pass electrolysis with adjusted H_2O flow rates for two-phase flow (−10.0 mA cm^{-2} single-pass electrolysis with 40.0 mL min^{-1} O_2).

hydrophobic CF provides abundant accessible active sites for O_2, while simultaneously enabling the H_2O_2 generated at these sites to be captured and carried away by the flowing H_2O phase. This promotes faster product extraction and real-time interface renewal, preventing further reduction of H_2O_2 at active sites. Notably, under optimized, truly electrolyte-free conditions (O_2: 40.0 mL min^{-1}, DI H_2O: 36.0 mL min^{-1}), the FE reaches 84.6% at −10.0 mA cm^{-2} (Figure 4d), confirming the system's core efficacy without electrolyte. The configuration also demonstrates robustness at an industrial current density, maintaining 82.4% FE at −100.0 mA cm^{-2} in 0.10 M $HClO_4$ (Figure S22). Collectively, the 3D flow-through architecture and two-phase flow dynamics establish a self-renewing triple-phase interface that fundamentally enhances H_2O_2 management efficiency.

Flexible Synthesis and Applications of H_2O_2

Building upon the optimized two-phase flow electrolysis system, we further developed an on-demand H_2O_2 synthesis technology and validated its potential for environmental remediation. It is realized by integrating the optimized two-phase flow electrolyzer with a T-junction microfluidic mixer (Figure 5a). Electrogenerated H_2O_2 solution is fed directly into dye solutions (e.g., methylene blue and malachite green), enabling on-site degradation of organic pollutants (Figure 5b,c). Under recirculating electrolysis at −10.0 mA cm^{-2} using 0.10 M $HClO_4$ as anolyte and DI H_2O/O_2 as catholyte, this system retains FE > 60% over 50 h (Figure 5d). Replacing the acidic anolyte with DI H_2O yields 67.9% FE, and using tap water/air feedstocks delivers 63.3% FE (Figure 5e), demonstrating robust performance across

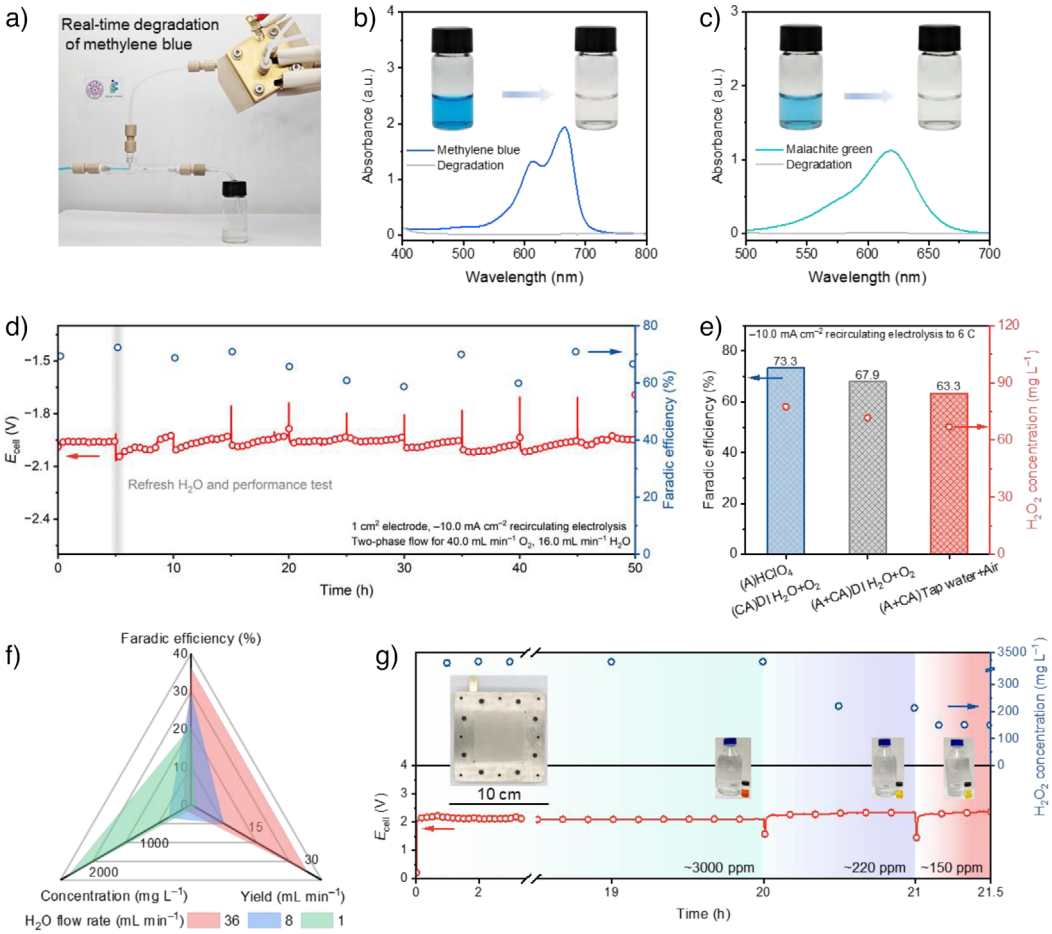

Figure 5. Flexible synthesis and application of pure H_2O_2 solution. a) Optical photo of the real-time degradation of methylene blue by TPI-MEA configuration with a T-junction microfluidic unit. b) UV–vis spectra and photographs of methylene blue and c) malachite green solutions before and after degradation. d) Stability test of the system at −10.0 mA cm^{-2}. E_{cell} represents the cell voltage. e) Multi-medium adaptability tests of the system. f) Radar chart of representative variables with adjusted H_2O flow rates in a 25 cm^2 electrolyzer (−50.0 mA cm^{-2} single-pass electrolysis with 200.0 mL min^{-1} O_2). g) Electrolysis curves and H_2O_2 concentrations for three types of two-phase flow rates in flexible electrosynthesis (−50.0 mA cm^{-2} single-pass electrolysis with 200.0 mL min^{-1} O_2 and 1.0/16.0/36.0 mL min^{-1} H_2O).

environmental media. Scale-up experiments (electrode area: 25 cm^2, Figure S23) demonstrate flexible tuning between high-concentration (2443.7 mg L^{-1} at 1.1 mL min^{-1}) and high-throughput (31.1 mL min^{-1} at 153.6 mg L^{-1}) modes via two-phase flow ratio control (Figure 5f and Table S4). To demonstrate the system's tunability and broad operational flexibility in the scaled-up device, we selected flow rates that encompass a stable two-phase flow regime: 200.0 mL min^{-1} O_2 with H_2O at 1.0, 16.0, and 36.0 mL min^{-1}. The variation in H_2O flow rate visually demonstrates the trade-off relationship between the concentration and the yield (Figure S24).

This enables tailored H_2O_2 production to meet diverse application demands: preparing 1 L of ~3000 mg L^{-1} pure H_2O_2 solution in 20 h or rapidly producing 1 L of ~150 mg L^{-1} low-concentration product within 30 min (Figure 5g). By uniquely decoupling concentration and throughput control through tunable gas–liquid ratios, our approach overcomes the inherent trade-off in single-phase PEM systems and affords truly flexible, on-demand H_2O_2 electrosynthesis under diverse operation conditions.

Conclusion

This work establishes a new and universal paradigm for electrolyte-free H_2O_2 electrosynthesis by combining triple-phase interface engineering with two-phase-flow dynamics in a zero-gap PEM electrolyzer. A 3D hydrophobic grid GDE drives alternating O_2/H_2O flows through its porous scaffold, simultaneously enhancing O_2 supply and H_2O_2 removal. CFD analysis validates that wake-induced vortices and interfacial shear synergistically boost dissolved-gas mixing and product convection. Using DI H_2O as the catholyte, the system delivers a high FE of 84.6% at −10.0 mA cm^{-2}. Beyond laboratory conditions, this platform enables real-time pollutant degradation via on-line microfluidic coupling and sustains 63.3% FE when operated with tap water and air. Scale-up to a 25 cm^2 electrode affords tunable H_2O_2 concentrations (153.6–2443.7 mg L^{-1}) and production rates (31.1–1.1 mL min^{-1}), decoupling throughput from concentration. This modular, water-and-air compatible design overcomes key mass-transfer trade-offs in conventional PEM systems and paves the way for

decentralized, on-demand H_2O_2 generation in environmental and industrial applications.

Acknowledgements

The authors acknowledge funding from the National Key Research and Development Program of China (2024YFE0211400), National Natural Science Foundation of China (22478221, 22408201, and 22521202), and China Postdoctoral Science Foundation (2023M741920, GZC20231259, 2025M771125, and GZC20250767). X.L. appreciates the Shuimu Tsinghua Scholar Program of Tsinghua University.

Conflict of Interests

The authors declare no conflict of interest.

Data Availability Statement

The data that support the findings of this study are available from the corresponding author upon reasonable request.

Keywords: Energy electrocatalysis · Hydrogen peroxide synthesis · Mass transfer enhancement · PEM electrolyzers · Triple-phase interface

[1] X. Li, C. Tang, L. Cong, K. Wu, J. Liu, J. Dong, S. Chen, Q. Zhang, *Angew. Chem. Int. Ed.* **2025**, *64*, e202510448, https://doi.org/10.1002/anie.202510448.

[2] L. S. Kriem, C. Pietzka, M. Beckett, L. Gärtling, B. Wriedt, *Agriculture* **2023**, *13*, 2122, https://doi.org/10.3390/agriculture13112122.

[3] Y. Ni, C. Zhou, M. Xing, Y. Zhou, *Green Ener. Environ.* **2024**, *9*, 417–434, https://doi.org/10.1016/j.gee.2023.01.003.

[4] Y. Huang, C. Zhang, X. Wang, Y. Wu, J. Lv, J. Zhang, W. Shen, X. Lu, *Nano-Micro Lett.* **2025**, *17*, 142, https://doi.org/10.1007/s40820-025-01657-9.

[5] H. Du, C. Li, Y. Liang, Z.-S. Wu, *J. Ener. Chem.* **2025**, *106*, 864–879, https://doi.org/10.1016/j.jechem.2025.01.059.

[6] X. Li, K. Wu, S. Chen, B. Yuan, J. Wang, C. Tang, Q. Zhang, *Chem Catal.* **2024**, *4*, 100997, https://doi.org/10.1016/j.checat.2024.100997.

[7] X. Li, L. Cong, H. Lin, F. Liu, X. Fu, H.-C. Xu, N. Lin, *Green Ener. Environ.* **2024**, *9*, 104–113, https://doi.org/10.1016/j.gee.2022.05.009.

[8] W. Liu, R. Chen, Z. Sang, M. Zheng, Z. Li, J. Nie, Q. Jiang, L. Yin, F. Hou, J. Liang, *J. Ener. Chem.* **2025**, *108*, 675–684, https://doi.org/10.1016/j.jechem.2025.04.058.

[9] C. Tang, Y. Jiao, B. Shi, J. N. Liu, Z. Xie, X. Chen, Q. Zhang, S. Z. Qiao, *Angew. Chem. Int. Ed.* **2020**, *59*, 9171–9176, https://doi.org/10.1002/anie.202003842.

[10] X. D. Zhu, Q. Zhang, X. Yang, Y. Wang, J. Wu, J. Gao, J. J. Zou, G. Wu, Y. C. Zhang, *SusMat* **2023**, *3*, 334–344, https://doi.org/10.1002/sus2.132.

[11] Y. Li, Y. Zhang, G. Xia, J. Zhan, G. Yu, Y. Wang, *Front. Environ. Sci. Eng.* **2021**, *15*, 1, https://doi.org/10.1007/s11783-020-1293-2.

[12] X. Zhang, Y. Xia, C. Xia, H. Wang, *Trends Chem.* **2020**, *2*, 942–953, https://doi.org/10.1016/j.trechm.2020.07.007.

[13] B. J. Su, J. J. Foo, G. Z. S. Ling, W. J. Ong, *SusMat* **2024**, *4*, e192, https://doi.org/10.1002/sus2.192.

[14] L. Cui, B. Chen, D. Chen, C. He, Y. Liu, H. Zhang, J. Qiu, L. Liu, W. Jing, Z. Zhang, *Nat. Commun.* **2024**, *15*, 10632, https://doi.org/10.1038/s41467-024-55091-3.

[15] E. Zhao, G. Xia, Y. Li, J. Zhan, G. Yu, Y. Wang, *ACS EST Eng.* **2023**, *3*, 1800–1812, https://doi.org/10.1021/acsestengg.3c00238.

[16] X. Ren, X. Dong, L. Liu, J. Hao, H. Zhu, A. Liu, G. Wu, *SusMat* **2023**, *3*, 442–470, https://doi.org/10.1002/sus2.149.

[17] C. Xia, Y. Xia, P. Zhu, L. Fan, H. Wang, *Science* **2019**, *366*, 226–231, https://doi.org/10.1126/science.aay1844.

[18] C. Liu, Y. Ji, T. Zheng, C. Xia, *JACS Au* **2025**, *5*, 521–535, https://doi.org/10.1021/jacsau.4c01183.

[19] E. Zhao, Y. Zhang, J. Zhan, G. Xia, G. Yu, Y. Wang, *Nat. Commun.* **2025**, *16*, 3212, https://doi.org/10.1038/s41467-025-58385-2.

[20] T. Ueki, M. Watanabe, *Macromolecules* **2008**, *41*, 3739–3749, https://doi.org/10.1021/ma800171k.

[21] Y. Wang, H. Yan, H. Fu, *eScience* **2025**, *5*, 100323, https://doi.org/10.1016/j.esci.2024.100323.

[22] Z. Xu, Z.-S. Wu, *eScience* **2025**, *5*, 100334, https://doi.org/10.1016/j.esci.2024.100334.

[23] Y. Chen, C. Zhen, Y. Chen, H. Zhao, Y. Wang, Z. Yue, Q. Wang, J. Li, M. D. Gu, Q. Cheng, H. Yang, *Angew. Chem. Int. Ed.* **2024**, *63*, e202407163, https://doi.org/10.1002/anie.202407163.

[24] I. Yamanaka, T. Murayama, *Angew. Chem. Int. Ed.* **2008**, *47*, 1900–1902, https://doi.org/10.1002/anie.200704431.

[25] F. Zhang, Z. Jin, C. Chen, Y. Tang, S. A. Mahyoub, S. Yan, Z. Cheng, *Ind. Eng. Chem. Res.* **2020**, *59*, 5664–5674, https://doi.org/10.1021/acs.iecr.9b07014.

[26] C. Tang, L. Chen, H. Li, L. Li, Y. Jiao, Y. Zheng, H. Xu, K. Davey, S.-Z. Qiao, *J. Am. Chem. Soc.* **2021**, *143*, 7819–7827, https://doi.org/10.1021/jacs.1c03135.

[27] Y. Tian, R. Chen, X. Liu, L. Yin, D.a. Yang, F. Hou, J. Liang, *EcoMat* **2023**, *5*, e12336, https://doi.org/10.1002/eom2.12336.

[28] Y. Wu, Y. Wang, R. Chen, J. Xu, Y. Wang, H. Zhang, Y. Ding, B. Li, S. Dong, S. Dou, X. Zhang, J. Sun, J. Sun, *Appl. Catal. B Environ.* **2024**, *343*, 123533, https://doi.org/10.1016/j.apcatb.2023.123533.

[29] X. Yuan, R. Zhou, M. Hu, X. Wu, Y. Du, Y. Ge, C. Yang, B. Jiang, R. Yang, *Ceram. Int.* **2025**, *51*, 35483-35495, https://doi.org/10.1016/j.ceramint.2025.05.269.

[30] Q. Zhao, J. An, S. Wang, Y. Qiao, C. Liao, C. Wang, X. Wang, N. Li, *ACS Appl. Mater. Interf.* **2019**, *11*, 35410–35419, https://doi.org/10.1021/acsami.9b09942.

[31] C. Li, H. Zhang, W. Liu, L. Sheng, M.-J. Cheng, B. Xu, G. Luo, Q. Lu, *Nat. Commun.* **2024**, *15*, 884, https://doi.org/10.1038/s41467-024-45179-1.

[32] Y. Cao, C. Soares, N. Padoin, T. Noël, *Chem. Eng. J.* **2021**, *406*, 126811, https://doi.org/10.1016/j.cej.2020.126811.

[33] I. Bagemihl, C. Bhatraju, J. R. van Ommen, V. van Steijn, *ACS Sustain. Chem. Eng.* **2022**, *10*, 12580–12587, https://doi.org/10.1021/acssuschemeng.2c03038.

[34] J. M. van Baten, R. Krishna, *Chem. Eng. Sci.* **2004**, *59*, 2535–2545, https://doi.org/10.1016/j.ces.2004.03.010.

[35] A. Etminan, Y. S. Muzychka, K. Pope, *Processes* **2021**, *9*, 870, https://doi.org/10.3390/pr9050870.

[36] F. Zhang, C. Chen, Y. Tang, Z. Cheng, *Chem. Eng. J.* **2020**, *392*, 124798, https://doi.org/10.1016/j.cej.2020.124798.

Manuscript received: September 09, 2025
Revised manuscript received: November 20, 2025
Manuscript accepted: November 24, 2025
Version of record online: November 28, 2025